Journal of the Mechanics and Physics of Solids 109 (2017) 34–49

Contents lists available at ScienceDirect

Journal of the Mechanics and Physics of Solids

journal homepage: www.elsevier.com/locate/jmps

The local strength of individual alumina particles

Václav Pejchal*, Marta Fornabaio, Goran Žagar, Andreas Mortensen

Laboratory of Mechanical Metallurgy, Institute of Materials, École Polytechnique Fédérale de Lausanne (EPFL), Station 12, CH-1015 Lausanne, Switzerland

ARTICLE INFO

Article history:
Received 23 April 2017
Revised 14 August 2017
Accepted 15 August 2017
Available online 18 August 2017

Keywords:
Alumina
Microscopic strength
c-shape
Micro-cantilever
Focused ion beam (FIB)

ABSTRACT

We implement the C-shaped sample test method and micro-cantilever beam testing to measure the local strength of microscopic, low-aspect-ratio ceramic particles, namely high-purity vapor grown α-alumina Sumicorundum® particles 15–30 μm in diameter, known to be attractive reinforcing particles for aluminum. Individual particles are shaped by focused ion beam micromachining so as to probe in tension a portion of the particle surface that is left unaffected by ion-milling. Mechanical testing of C-shaped specimens is done *ex-situ* using a nanoindentation apparatus, and in the SEM using an *in-situ* nanomechanical testing system for micro-cantilever beams. The strength is evaluated for each individual specimen using bespoke finite element simulation. Results show that, provided the particle surface is free of readily observable defects such as pores, twins or grain boundaries and their associated grooves, the particles can achieve local strength values that approach those of high-perfection single-crystal alumina whiskers, on the order of 10 GPa, outperforming high-strength nanocrystalline alumina fibers and nano-thick alumina platelets used in bio-inspired composites. It is also shown that by far the most harmful defects are grain boundaries, leading to the general conclusion that alumina particles must be single-crystalline or alternatively nanocrystalline to fully develop their potential as a strong reinforcing phase in composite materials.

1. Introduction

Particle fracture is well-known to be one of the primary causes for the premature failure of particulate composites or multiphase alloys (Babout et al., 2004; Beremin, 1981; Brechet et al., 1991; Ghosh and Moorthy, 1998; Gurland, 1972; Lewandowski et al., 1989; Li et al., 1999; Llorca et al., 1993; Mummery et al., 1993; Mummery and Derby, 1994; Pandey et al., 2000; Scarber and Janowski, 2001). It is also known, from both experiment (Bonderer et al., 2008; Bouville et al., 2014; Hauert et al., 2009a; Kouzeli et al., 2001; Krüger and Mortensen, 2014; Le Ferrand et al., 2015; Miserez et al., 2006, 2004a, 2004b; Miserez and Mortensen, 2004; Munch et al., 2008) and micromechanical theory (Hauert et al., 2009b; Tekoglu and Pardoen, 2010), that stronger, more ductile, and tougher particulate composites are produced if the intrinsic strength of their particulate reinforcement is increased.

It is in this light surprising that so little attention has been paid to quantifying the strength of hard particles used in composites or found as coarse precipitates in alloys. One of the main reasons for this is that the strength of a particle is

* Corresponding author.
E-mail addresses: vaclav.pejchal@epfl.ch, vaclav.pejchal@alumni.epfl.ch (V. Pejchal).

http://dx.doi.org/10.1016/j.jmps.2017.08.005
0022-5096/

inherently difficult to measure since, unlike a fiber, it cannot be gripped. To date the strength distribution of particulate reinforcements has generally been estimated indirectly, by coupling more or less elaborate micromechanical models of two-phase composite material behavior with direct or indirect observations of particle fracture (Babout et al., 2004; Brockenbrough and Zok, 1995; Caceres and Griffiths, 1996; Eshelby, 1957; Hauert et al., 2009a; Kiser et al., 1996; Lewis and Withers, 1995; Li et al., 1999; Majumdar and Pandey, 2000; Mochida et al., 1991; Wallin et al., 1986; Wang, 2004; Wang et al., 2003) or using X-ray and neutron diffraction to estimate average strains in reinforcing particles at the onset of particle cracking (Coade et al., 1981; Finlayson et al., 2007; Mueller et al., 2008).

Comparatively, only a few studies report direct measurements of the fracture stress in individual reinforcing particles. Pioneering efforts can be found in Harris et al. (2007), Joseph et al. (2015), Ogiso et al. (2007), Webb and Forgeng (1958) and Yoshida et al. (2005). Newer techniques give access to more direct measurements, free of extraneous flaws that were often introduced in the particles in earlier methods. Recent developments in three-dimensional synchrotron X-ray diffraction enable now the determination of micrometer-scale grain-resolved elastic strains within multiphase materials (Sedmák et al., 2016); however, to the best of our knowledge this technique has not been used to measure the local stress at fracture in reinforcing particles. Another recent method used to measure the strength of individual microscopic particles combines focused ion beam machining (FIB) with microscopic particle bending tests (Feilden et al., 2017; Mueller et al., 2016). This approach provides access to unambiguous strength data of individual reinforcement particles; however, it is only suitable for particles of relatively high-aspect ratio, i.e., for fibers or platelets.

We present here an alternative micromechanical testing approach, which also uses FIB-shaped samples and measures the local strength, directly and free of micromilling artifacts, in the surface region of particles of almost any convex shape. The approach is inspired from the parallel problem of mechanical characterization of ceramic bearings (Strobl et al., 2014; Supancic et al., 2009; Wereszczak et al., 2007a, 2007b), which we have recently extended to the microscale and demonstrated by measuring the local strength of strong and brittle reinforcing fibers embedded in a metal (Žagar et al., 2015). Here we extend this approach towards testing microscopic particulate composite reinforcements of irregular shape and low aspect ratio. Specifically, we report here observations of directly determined strength measurements conducted on Sumicorundum® (Sumitomo Chemical Co. Ltd., Tokyo, Japan) alumina particles of diameter in the range 15–30 μm, which have been shown to provide superior reinforcement in infiltrated aluminum- or copper-based metal matrix composites (Kouzeli et al., 2001; Krüger and Mortensen, 2014; Miserez et al., 2006, 2004a; Miserez and Mortensen, 2004). As will be seen, the measured strength of the alumina particles can be higher than what is measured for high-strength nanocrystalline alumina fibers, or in alumina platelets a few hundred nanometers thick that have been used in bio-inspired composites. Their strength approaches that of high-perfection alumina whiskers and microcrystals where specific defects are absent. We identify those specific defects as: (i) grain boundaries and grain boundary grooves, (ii) micropores and (iii) other shape irregularities. We show that random grain boundaries are particularly deleterious to the strength of alumina particles, leading to an overall conclusion that alumina has great potential as a particulate reinforcement in composite materials provided it is (i) smooth in shape and (ii) single- or nano-crystalline.

2. Materials and methods

2.1. Material

Particles investigated in this work were high-purity α-alumina particles (AA-18, Sumicorundum® grade) produced by Sumitomo Chemical Co. Ltd. (Tokyo, Japan) by in-situ chemical vapor deposition. The typical particle size is between 15 and 30 μm (Uchida et al., 1995). XRD analysis performed in our laboratory confirmed that the particles are entirely of α-alumina. Chemical analysis provided by the manufacturer states as main impurities Si ($<$ 50 ppm), Fe ($<$ 20 ppm), Na ($<$ 15 ppm), Mg ($<$ 10 ppm), and Cu ($<$ 10 ppm). The as-received powder particles have polyhedral shapes and consist generally of (i) single crystal particles with a low aspect ratio or (ii) particles consisting of two or more polyhedral crystallites linked along a grain boundary, which forms a groove at the particle surface. By investigating 200 SEM images of random Sumicorundum particles from this study, we estimate that roughly half of all the particles are single-crystalline while the other half is made of two or more crystallites forming grain-boundary grooves.

2.2. Micromechanical testing

2.2.1. C-shaped particle test method

To measure the local strength of the particles we extend to particles the approach presented in Žagar et al. (2015). The approach requires having particles partially embedded in a matrix that holds each particle in place during load application. To this end, a Sumicorundum particle – polymer matrix composite with a low fraction of the alumina particles (a few percent) was produced. The polymer matrix was then deep-etched, or alternatively in one specimen it was cracked, so as to cause particles partially embedded in the matrix to protrude by several micrometers out of the matrix. To prevent sample charging the FIB/SEM and to protect the surface of particles from FIB damage and/or redeposition, the sample with partially embedded particles was coated with $\approx$40 μm of thermally evaporated carbon. Selected particles were FIB milled to form a C-shaped particle specimen, outlined in Fig. 1 and featuring (i) two parallel and roughly vertical sides, (ii) a wide rectangular notch machined with the beam oriented perpendicular to the previously machined sides, and (iii) a roof situated at the top

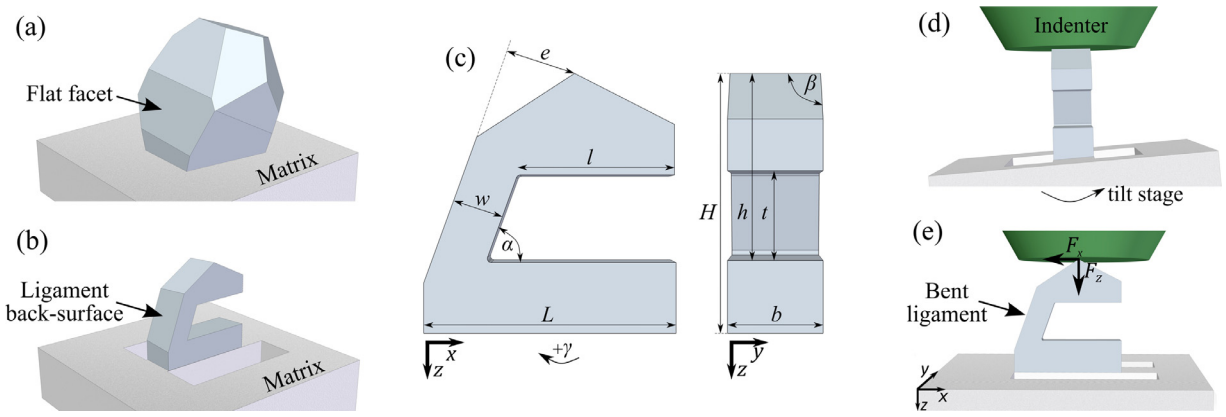

Fig. 1. Schematic representation of a C-shaped particle test. (a) A polyhedral Sumicorundum particle partially embedded in a polymer matrix is (b) FIB machined into a C-shape configuration, and then tested in compression to bend a ligament of rectangular cross-section. The back surface of the ligament is left unaffected by the FIB milling operation, by design of the machining process and by coating the particle surface with a layer of weak carbon ≈40 nm thick. The roof machined at the top of the particle defines the load application line. (c) Sketch of a notched specimen with dimensions defined. (d) As a result of the machining process, the roof and notch side are oriented at a shallow angle ($< 5°$) with respect to the matrix free surface normal (see Appendix), such that the roof-edge and indenter can be aligned using a tilt stage so as to be parallel in the nanoindentation apparatus prior to testing. (e) Once the notched specimen is loaded by applying a vertical displacement (along the *z*-axis), the roof slides laterally along the flat indenter surface, introducing a measurable friction force in the lateral direction (along the *x*-axis).

of the particle cut parallel to the notch. The wide rectangular notch is machined in such a way that one of its sides is aligned parallel with a selected facet of the polyhedral particle (Fig. 1a). This, together with the two FIB milled sidewalls and the vertical portion of the machined C-notch, forms what we call hereafter the *ligament* of C-shaped particle specimens. This ligament has a rectangular cross-section (Fig. 1b).

This FIB-machined C-shaped specimen, sketched in Fig. 1c, is then tested using a TI 950 TriboIndenter™ (Hysitron Corp., Minneapolis, MN, USA) nanoindentation apparatus equipped with a ≈10 μm tip diameter flat-end diamond probe and with a 3D OmniProbe™ transducer capable of measuring vertical and lateral force simultaneously. Prior to testing, the roof of the C-shaped specimen is aligned parallel to the 3D OmniProbe flat-end diamond probe using a tilt stage fixed on the nanoindenter base stage (Fig. 1d). As the C-shaped particle specimen is loaded vertically by the flat-end diamond probe, its ligament bends, causing the appearance of high tensile stresses along the back-surface of the ligament. While the ligament bends, the specimen roof moves laterally and slides along the flat-end diamond probe, causing the appearance of a lateral friction force between the edge of the roof and the diamond. Using a multidirectional nanoindentation probe this lateral force was measured, to derive a friction coefficient, which was taken into account in data analysis (Fig. 1e); see also Ref. (Žagar et al., 2015). Further details of the C-shaped particle test are provided in the Appendix.

Besides particles with a flat facet and free of any visible defects, several particles containing flaws of different nature along the ligament back surface to be subjected to tension during the test were prepared. These included particles with twinned jagged surfaces, and particles with grain boundary grooves; the latter were found to exert a particularly deleterious effect on the local particle strength. In a few additional specimens, the back-surface of the ligament was also FIB-machined in order to (i) compare strength results against specimens with an outer ligament surface in pristine (FIB unaffected) condition, (ii) probe the strength governed by pores revealed during sample preparation or (iii) determine the strength of particles containing a grain boundary free of the groove that is generally associated with the emergence along a free surface of such a grain boundary.

2.2.2. Micrometric bend beams

An alternative approach is to carve microscopic cantilever beams out of individual particles. This approach is suitable if one wishes to probe facets or features along a particle surface that is oriented roughly parallel to the polymer matrix free surface. Two such cantilever beams, both containing a grain boundary groove at the junction of two grain facets, were machined and tested. A sketch of the cantilever beam configuration used in this work, showing sample dimension definitions, is given in Fig. 2. In both cantilever specimens the top surface of the cantilever beam, subject to tension during the test, was left unaffected by FIB milling. These beams were then mechanically tested in-situ in the SEM using a FemtoTools FT-NMT03 Nanomechanical Testing System (Buchs-ZH, Switzerland) similarly to the tests exposed for Si particles in aluminum in Mueller et al. (2017). Further details of particle cantilever beam specimen preparation and testing are given in the Appendix.

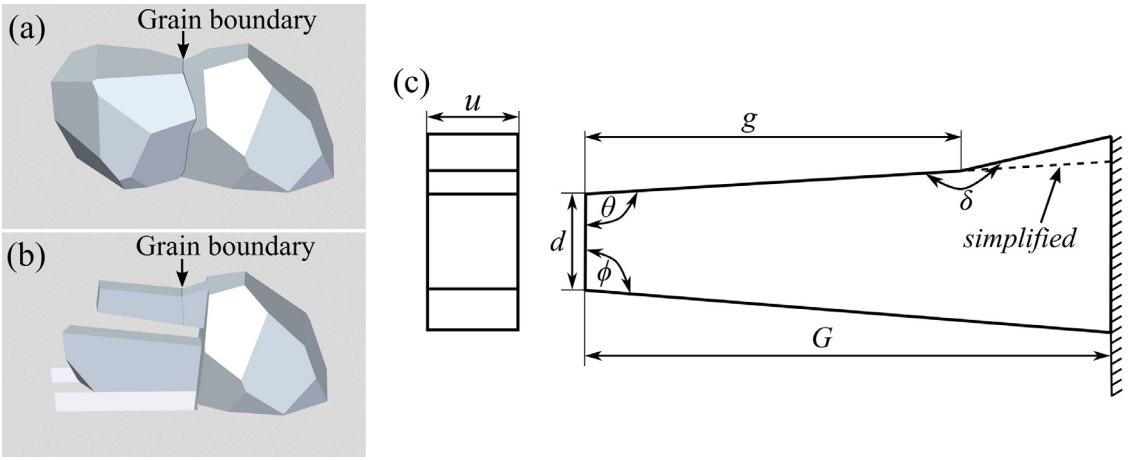

Fig. 2. (a) A partially embedded Sumicorundum particle containing a grain boundary is (b) FIB milled to form a micro-cantilever that contains the grain boundary. The top surface of the micro-cantilever subject to tension during mechanical testing is left in its pristine condition, meaning unaffected by FIB. (c) Sketch of a cantilever beam geometry used in the work with definition of relevant dimensions. The edge defined by angle δ is formed where two particle facets meet. The dashed line represents the simplified beam geometry in which the geometry-related stress concentration is eliminated.

2.3. Finite Element (FE) simulation

The material forming the Sumicorundum alumina particles is α-alumina, which is an anisotropic material characterized by six elastic constants. Because the exact crystal orientation of each particle was not determined, we assimilated the particles to an isotropic material having the orientation-averaged Young's modulus, $E = 400$ GPa, and Poisson's ratio, $\nu = 0.25$, of polycrystalline alumina (Dörre and Hübner, 1984; Wachtman et al., 1960). The sensitivity of the computed stress fields on the range of values for the Young's modulus and Poisson's ratio (realistic upper and lower bounds of alumina) is on the order of 5% of the computed value; see the Supplementary information.

Each individual C-shaped test specimen was simulated by means of a bespoke quasi-static two-dimensional plane-strain Finite element model (FEM), implemented in the Abaqus/Standard™ 6.11 software (Dassault Systèmes, Providence, RI, USA); see Fig. 7a. The bottom surface of the visible part of the particle that is sticking out of the polymer was constrained by an encastre boundary condition (all displacements and rotations are zero). The loading was prescribed at the roof edge with vertical F_z and lateral F_x force values measured in the experiment. The FEM analysis included non-linear geometric effects (big displacements). Elements used for discretization of the particles were 2nd order quadrilaterals (CPE8).

The 2D model, for one particular C-shaped specimen of representative geometry, was compared against a more realistic three-dimensional (3D) model of the same geometry (see Fig 7b). The 3D model consists of the alumina particle embedded within an isotropic, linear elastic polymer-like matrix of Young's modulus ~1 GPa (this value was inferred from an independent nanoindentation experiment conducted by ourselves on the polymer used to fix the particles). The Poisson's ratio of our polymer matrix was not determined; however, calculations show that its effect on the stress distribution within the particle ligament is negligible; thus we use a default value of 0.25. The interface between the particle and the matrix was considered as being a fully coupled (tie) contact. The bottom of the matrix was encastred. Elements used in discretizing the particle and the matrix in the 3D model were second order bricks, C3D20 and C3D20R, respectively.

The two cantilever beam tests were analyzed by means of 3D cantilever finite element models reconstructed from the geometrical measurements of samples. Both cantilever beam parts that represent in reality different alumina particles (of possible different orientation) were assimilated to the same effectively isotropic alumina material described above. Cantilever beams and supports to which the cantilevers are attached were modeled using C3D20 and C3D20R elements, respectively. A more refined mesh was constructed near the location of particle boundary and near the cantilever's fixed ends. Only the portion of the cantilever from the fixed point up to the point of the load application was considered in the model. Loading was produced by prescribing the vertical point load at the free cantilever end, the force at which (load at failure) is measured by experiments. The bottom of the support was fixed by encastre boundary condition.

Tested cantilever specimens both contained a grain-boundary where two facets meet forming an edge-like feature at the top surface, situated a few hundred nanometers from the beam support and characterized by the angle δ (Fig. 2). The presence of the edge results in a local stress concentration ($\delta > 180°$) or dip in stress ($\delta < 180°$) along the beam top surface. The effect of this edge can be assimilated to that of a notch or protrusion. To evaluate the strength of tested beams with the edge assimilated to a geometrical flaw, we employed a simplified model in which the beam's top surface was taken to be entirely flat by extending the top portion of the beam on the left-hand side of the edge towards the cantilever support ($\delta = 180°$); this is also sketched in Fig. 2c. The model then gives the nominal stress state along the beam surface treated as a flat surface along which the geometrical stress concentration site is but one of a variety of possible failure-producing flaws.

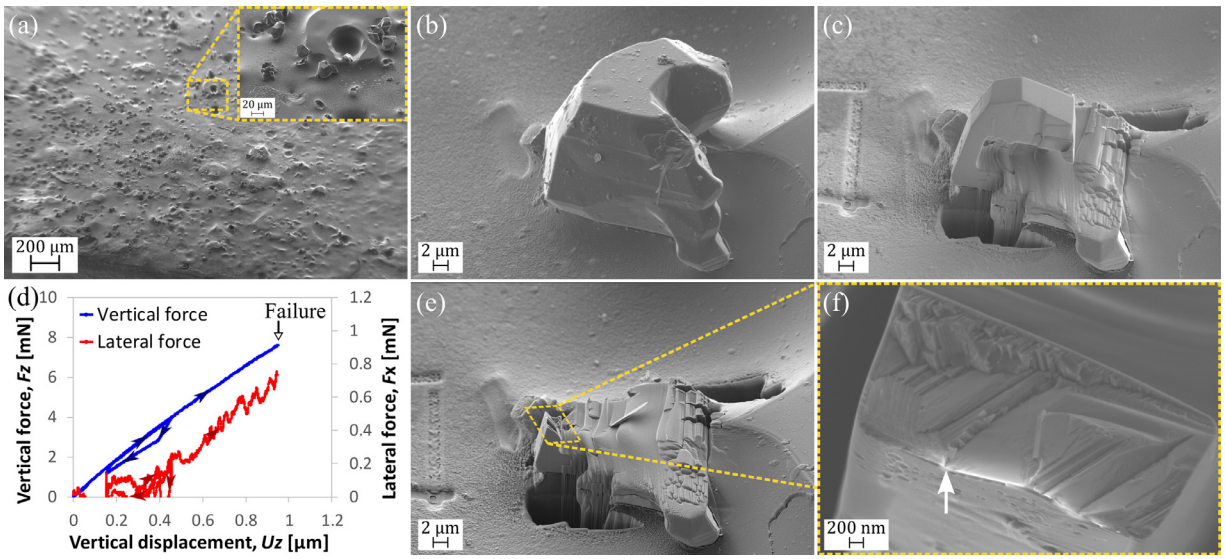

Fig. 3. C-shaped particle test of a typical single-crystalline Sumicorundum AA-18 particle with the ligament back-surface in *pristine* condition, free of FIB damage and apparent defects (Category I, Specimen I-4). (a) SEM image of a polymer-matrix composite sample with particles partially embedded in the matrix after deep-etching. SEM images of the selected particle (b) before and (c) after FIB machining. (d) Vertical and lateral force vs. vertical-displacement response of the notched particle during the test. (e) SEM image of the particle after the test and (f) close-up of the fracture surface with an arrow indicating the apparent failure initiation location suggested by river-markings observed on the fracture surface.

3. Results

3.1. Mechanical testing

The deep-etching sample preparation procedure provided a number of partially embedded particles situated far enough from neighboring particles to be readily available for FIB machining. Fracturing the polymer composite provided on the other hand only a few partially embedded particles ready for FIB milling. This was mainly due to the partial sedimentation of particles at the bottom of the sample during polymer curing. Therefore, only one tested particle in this work was prepared by the fracturing method. The polymer-particle interface was found to be sufficiently strong to keep particles in place while performing the mechanical tests.

Apart from grain boundary grooves, Sumicorundum particles do not contain readily observable flaws along their surface. Cutting particles by FIB-milling during sample preparation revealed, however, that some particles contain pores of diameter in the range from a few tens to a few hundred nanometers. Pores were observed within individual crystallites as well as along alumina grain boundaries.

In total, seventeen (17) C-shaped particle specimens and two (2) in-situ SEM micro-cantilever beams were tested to fracture; specifics of each specimen are provided in the Supplementary information. Based on the flaws observed before or after testing and the state of the ligament back-surface, the tested specimens were catalogued into the following six categories: we have tested

(i) five specimens of single crystal particles with the ligament in pristine condition, free of any visible defect (Category I) (Fig. 3b),
(ii) two specimens of single crystal particles with the ligament free of any visible defects and FIB machined from all sides including the ligament back-surface (Category II) (Fig. 5a),
(iii) three specimens of single crystal particles featuring a pore along the ligament (Category III) (Fig. 5b),
(iv) one particle with a twinned jagged ligament back-surface (Category IV) (Fig. 5c),
(v) five specimens of polycrystalline particles with all sides machined using the FIB (Fig 6a), including the ligament back-surface, and containing a grain boundary oriented roughly normal to the principal tensile stress direction during the test (Category V) and
(vi) one C-shaped particle specimen and two micro-cantilever specimens containing a grain boundary groove along a ligament surface that was left unaffected by focused ion beam milling (Category VI) (Fig 6b).

Fig. 3 summarizes the course of a typical C-shaped particle test, conducted on a specimen of Category I; namely, a single-crystalline particle with its ligament free tensile surface left in pristine condition without any visible defects. Fig. 3a represents an overview of the polymer matrix composite after deep etching with the “piranha solution” followed by carbon coating. Partially embedded Sumicorundum alumina particles are readily observable. The selected polyhedral particle for C-shape testing exhibiting a flat facet oriented roughly vertical to the polymer free surface is highlighted in the figure. Fig. 3b

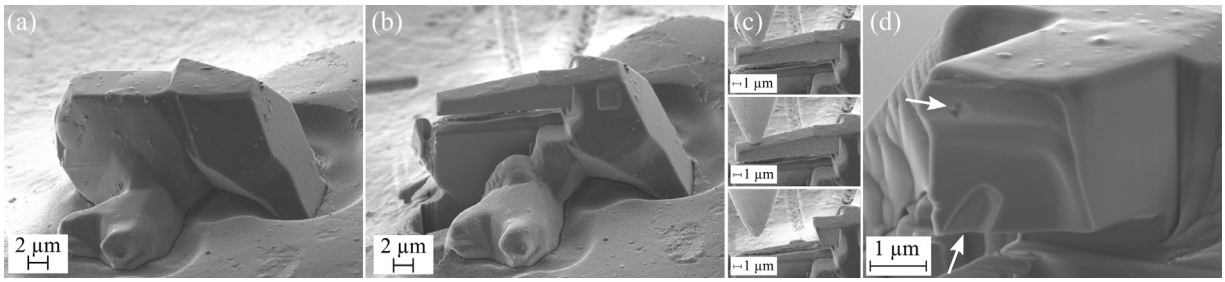

Fig. 4. Summary of cantilever beam testing of a Sumicorundum AA-18 particle containing a grain-boundary groove (Category VI, specimen VI-3). SEM micrographs of (a) selected particle before and (b) after FIB machining. (c) Three frames during the in-situ SEM test using nanomechanical testing instrument equipped with sharp tungsten needle. (d) Close-up of the fracture surface of the beam after the test with arrows indicating two observed pores in the fracture surface.

and c represent the selected particle before and after FIB machining, respectively. The vertical force – vertical displacement as well as lateral force – vertical displacement response recorded during the test, shown in Fig. 3d, exhibit a hysteresis loop produced during one load–unload cycle before the force was ramped up until failure occurred. The hysteresis is due to sliding of the specimen's roof along the flat-end diamond indenter; this is characteristic of the C-shaped sample test method, see Ref. Žagar et al. (2015). The value of the friction coefficient, defined as the measured ratio F_x/F_z, was approximately 0.09. A sudden drop in load and jump in displacement are indicative of specimen failure.

The relatively low loads at which the ligament breaks does not produce extensive shattering of the ligament; hence, fractographic examination of the samples could usually be performed (Fig. 3e,f). The specimen in Fig. 3f exhibited a heavily faceted fracture surface with no apparent flaw. A pattern of radial ridges observed around the area indicated by the white arrow in the figure suggests that failure initiated near or at the indicated spot. This is an important observation as the failure did not initiate in one of the FIB-machined corners; rather, failure had its origin at or near the surface unaffected by FIB micromaching.

Of the other Category I specimens, one (Specimen I-1) led to a similar conclusion, namely that failure initiated away from the FIB-affected ligament surface. The other three Category I specimens could not be examined for fractography because the fracture surface was situated below the specimen ligament, with the crack trajectory connecting the bottom corner of the specimen rectangular notch with the surface of the particle on the other end (see Fig. S1a,b in the Supplementary information). This indicates that failure initiated either at (i) a greater flaw remote from the region of peak stress, situated along or just under the specimen surface below the ligament or (ii) along the highly stressed ligament surface followed by subsequent initiation and growth of secondary cracks, possibly emanating from roots of the notch corners where the comparatively small radius of curvature of few hundred nanometers (typically 200 nm–500 nm) is likely to have concentrated post-fracture stress waves, leading to a loss of the original fracture surface. Two observations suggest that option (ii) is more plausible. First, we have observed no sign of a bigger flaw in the remaining fracture surfaces and secondly, in the specimens that broke within the ligament, we observed the presence of microcracks having their origin in the bottom corner of the specimen notch, which grew for a few hundreds of nanometers towards the other end, along a direction such that they would end below the actual ligament were their growth to continue across the specimen, giving the specimen remainder the shape that was observed in the last three Category I specimens (see Fig. S1c,d in the Supplementary information).

Fig. 4 summarizes the preparation and mechanical testing of one of the micro-cantilever beam specimens. Fig. 4a and b display the selected particle before and after FIB machining, respectively. The beam was machined such that the grain boundary is contained within the beam and is oriented roughly perpendicular to the beam longitudinal axis (Category VI). The grain boundary groove was left roughly 2 μm away from the beginning of the support. Fig. 4c represents three frames from the recorded video of the test; the beginning of the test, the beam loaded just before failure, and the specimen after failure. One part of the fractured beam is missing because it was ejected during the test (due to the sudden release of stored elastic energy). The testing instrument recorded the load at which the beam failed. The load–displacement response was linear until failure, which was manifest as a sudden drop in load.

Fig. 4d displays the fracture surface after the test. The fracture surface is very different from the other fracture surfaces of tested single-crystalline particles: it is smooth throughout the whole surface, indicating that the crack propagated within the grain boundary. The test also reveals the profile of the grain boundary along the beam cross-section: as seen, it is not perfectly flat. It was impossible to identify the fracture initiation site on this almost featureless fracture surface. Two flaws, one smaller pore $\approx$ 300 nm in diameter and one elongated pore (partially cut by FIB machining) with its size on the order of 1 μm, were observed. The bigger pore was located in the portion of the beam that was in compression. Examples of tested particles from other categories, along with fractography, are documented in Figs. 5 and 6.

An example of a fully FIB-machined single crystalline specimen (Category II) is shown in Fig. 5a1–a3. The surface crystallographic orientation was kept the same as the original pristine surface by FIB milling the ligament back-surface with FIB beam oriented parallel to the original surface. The fracture surface was, as for Category I specimens, heavily faceted with

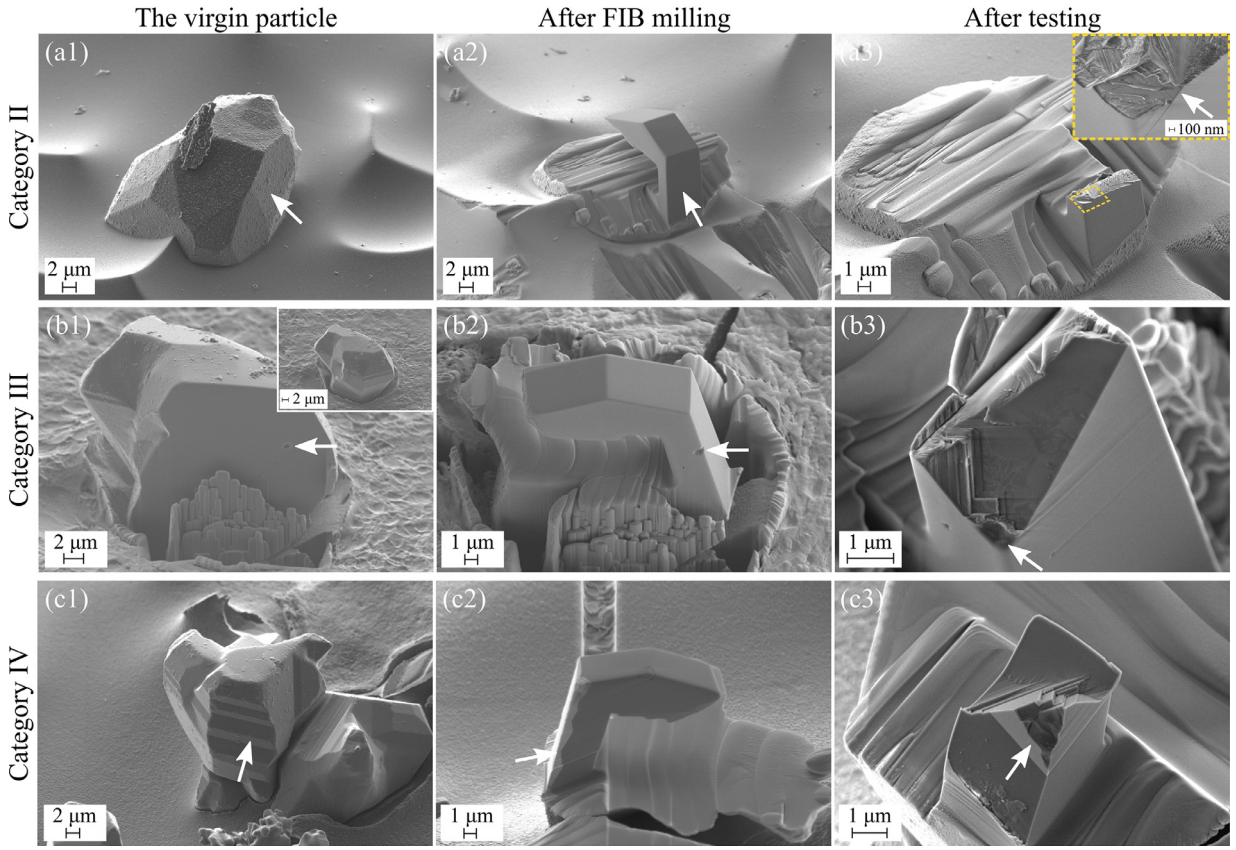

Fig. 5. Overview of tested representative specimens from (a) Category II (II-1), (b) Category III (III-1), and (c) Category IV (IV-1). (a1-2) A few hundred nanometers of pristine ligament back-surface were milled away with the focused ion beam parallel to the original surface. (a3) Radial ridges observed on the fracture surface suggest fracture initiation (arrow). (b1) A pore ≈800 nm in diameter (arrow) was revealed while machining the sides. (b2) The outer ligament surface was also FIB machined in order to locate the pore close to the ligament surface where the tensile stress peaks during the consequent mechanical test. (b3) Close-up of the fracture surface after the test with fractographical features suggesting that the pore was indeed the origin of the failure. (c1) Twinned surface specimen before and (c2) after FIB machining with visible re-deposition of material on the ligament back-surface. (c3) The same specimen after the test with its fracture surface: re-deposited material has delaminated during the mechanical testing.

radial ridges indicating the site of failure initiation. Additionally, two microcracks could be observed after the test on the ligament back-surface close to the failure initiation oriented roughly at 45° to the horizontal plane of the ligament.

Fig. 5b1–b3 shows a Category III particle containing a pore approximately 800 nm in diameter along the specimen's ligament surface. The pore was exposed during the FIB machining of one of the side edges of the particle, during the initial stage of the C-shaped specimen preparation (Fig. 5b1). The back surface of the specimen ligament was then FIB machined in order to locate the pore close to its surface subjected to tension during the test. Fractography revealed that particle failure most likely initiated from the pore, and the fracture surface exhibited steps as in the previous single-crystalline particles of Category I and II. Another example of a tested particle containing a pore is presented in Fig. S2 in the Supplementary information. In that sample, the pore was only revealed after the test, as it was fully contained within the ligament (note that therefore the material in and near the pore free surface, where the failure initiated, was not exposed to FIB milling).

Fig. 5c1–c3 presents a tested particle with a twinned, jagged, surface. Redeposition of material after milling on the back-surface of the ligament is evident. After mechanical testing the redeposition layer was absent: it had apparently delaminated, suggesting that the carbon layer played its role in providing a weak interface between the particles and any redeposited material. The fracture surface exhibits again crystallographic steps.

Fig. 6a1–a3 displays a tested polycrystalline Sumicorundum alumina particle having one grain-boundary with its plane roughly parallel to the polymer free surface. The back-surface of the ligament containing the grain boundary was machined flat by ion-milling, so as to eliminate the grain boundary groove and associated stress concentration. This specimen belongs to Category V. Similar to the Category VI micro-cantilever beam specimen, the fracture surface is very smooth and feature-less throughout the whole surface, indicating that the crack propagated within the grain boundary. A minute pore with a diameter of approximately 200 nm was observed and located in the region of the ligament cross-section that was under compression during the test; therefore, it is unlikely that failure initiated there.

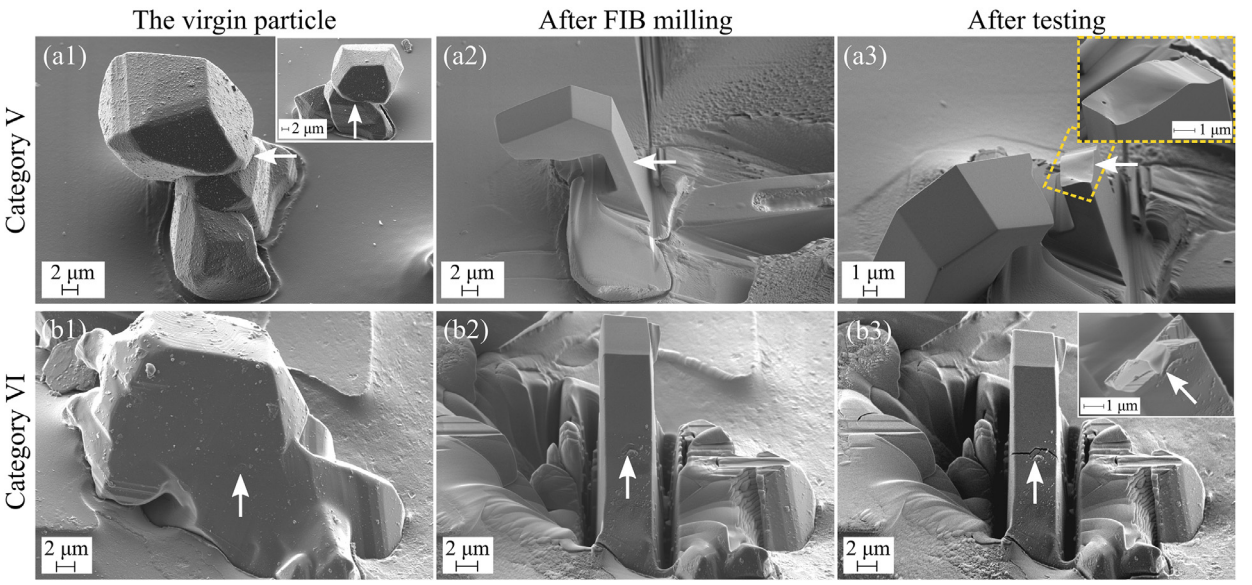

Fig. 6. Overview of tested representative specimens from (a) Category V (V-3) and (b) Category VI (VI-1). (a1) A specimen with a grain-boundary oriented roughly horizontal to the free-surface of the polymer matrix and (a2) contained in the ligament with all four sides machined by FIB and therefore a flat ligament back surface (without grain-boundary groove). (b1) The only C-shape specimen from the Category VI with a grain boundary groove. (b2) Specimen contained the grain boundary within its ligament after FIB machining. Compared to the other two specimens from Category VI tested in the cantilever beam configuration, the grain boundary extends only through a portion of the ligament cross-section; see (b3).

Fig. 6b1–b3 shows the tested C-shape specimen containing a FIB unaffected grain-boundary groove. The grain that formed the grain boundary groove visible along the surface was much smaller than the rest of the particle, and hence essentially represented an inclusion. As a consequence the fracture surface displays a combination of (i) heavily faceted region of the parent single-crystalline particle and (ii) smooth featureless surface typical of a fractured grain boundary. EDX analysis did not reveal any chemical composition difference of the inclusion grain.

3.2. FEM analysis

3.2.1. C-shaped particle test analysis

Fig. 7a displays a simplified 2D plane-strain model of a representative C-shaped test specimen, together with its dimensions (I-2). Fig. 7b represents the same particle simulated using a Full 3D FE model that includes the portion of the particle embedded in the polymer matrix. Fig. 7c shows the vertical force – vertical displacement from the experiment together with the response from the 2D and 3D models of the same C-shape specimen. The curve predicted by a second 3D model is also included: with this model, the (3D) emerging portion of the sample is fully clamped at the bottom where it enters the polymer matrix, such that it has the same boundary condition as the 2D model. As seen, both fully clamped (2D and 3D) models come close to one another (such that simplifying the 3D beam as a 2D plane strain beam has little importance), and exhibit a somewhat stiffer force–displacement response compared to the experimental curve. Modeling the polymer matrix and embedding the 3D model in it, the resulting force-displacement response shifts downwards and follows relatively well the experimental curve. It is now slightly more compliant; however, the agreement also for the 2D model is satisfactory, considering simplifications made, such as the somewhat simplified geometry of the bottom of the particle and the approximation used for the size of the particle portion that is embedded in the matrix. More importantly, the sensitivity of the computed stress field on the exact model used (2D vs. 3D) was found to be negligible: a full 3D representation of the stress field and including the polymeric matrix in the simulation matters more in computing the overall particle compliance than it does in computing its peak stress distribution. Fig. 7d compares the distribution of the first principal stress along the mid-plane of the ligament back surface from the two models at the moment of failure. As is evident, the stress distribution is insensitive to the model used, and the simplified 2D plane-strain model provides an equally good stress analysis along the particle ligament free surface as the more realistic but also more complex 3D model. This result also indicates that most of the extra compliance in the force–displacement response between the two models comes from an elastic vertical sink-in of the specimen into the polymer, rather than from rotation of the specimen around the y-axis, as this would affect the bending moment from the applied forces, inducing in turn a visible redistribution of the stress in the ligament.

3.2.2. In-situ bend beam analysis

The two tested specimens contained two facets forming an edge (see Figs. 4 and 8). By considering the edge as a geometric flaw we estimated the nominal strength of the present specimen material. To this end, we used a simplified beam

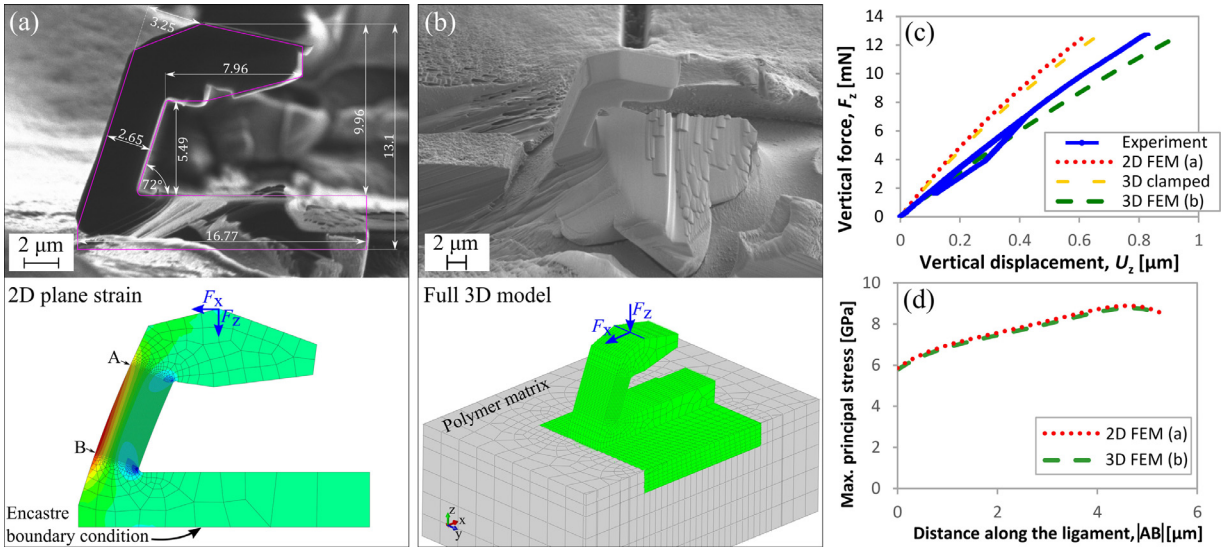

Fig. 7. FEM simulation of a C-shaped specimen test with representative particle dimensions (I-2). (a) Simplified 2D plane strain FEM model of the particle with dimensions visible by imaging from its side and with encastre boundary condition at its bottom. (b) The full 3D FEM model of the same particle takes into account the portion of the particle embedded in the polymer matrix. (c) The load–displacement curves from (blue) experiment, (dashed-green) the 3D FEM model including the polymer matrix, (dotted-red) the 2D plane-strain FEM model, and 3D model with the same boundary conditions as for the 2D model. A loop in the experimental curve represents one load–unload cycle conducted before the displacement was ramped-up all the way to failure. (d) Comparison of the distribution of the maximum (tensile) principal stress along the ligament outer surface of the full 3D and 2D FEM model loaded with the pair of vertical and lateral force (F_x, F_z) measured at the moment of failure in the experiment. (For interpretation of the references to color in this figure legend, the reader is referred to the web version of this article).

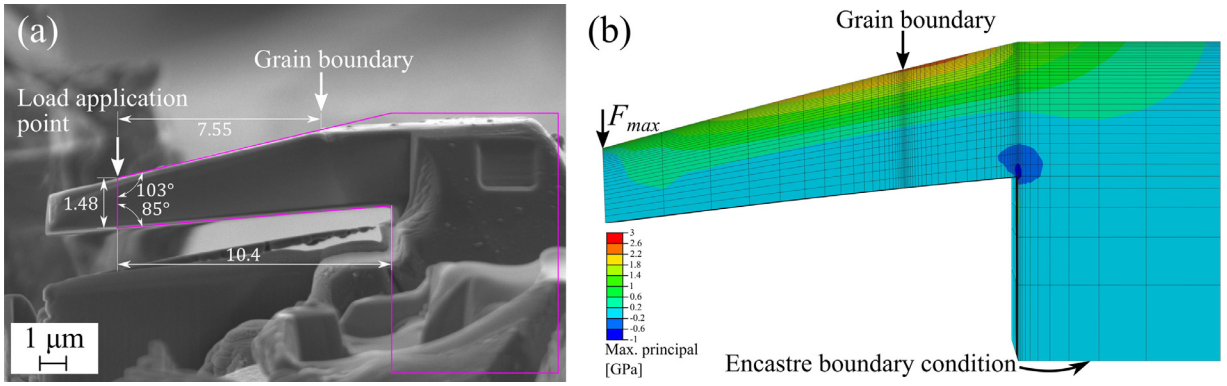

Fig. 8. FEM model of the cantilever beam from Fig. 4 with visible grain-boundary groove. (a) Dimensions used to produce (b) the 3D FEM model. Note that the simplified beam geometry was used with the beam's top surface flat as outlined in Section 2.2.2 (Fig. 2). The strength of the specimen evaluated as the first principal stress at the position of the grain-boundary groove was 2.3 GPa.

model, as exposed in Section 2.2.2, in which the beam top surface was taken to be entirely flat (Fig. 8). By doing this, calculated stresses in the beam just past the edge on the right-hand side are not representative; however, on the left-hand side and in the region surrounding the grain boundary and edge (this being where failure took place) the simplified model gives representative nominal stresses within the beam, which were computed as the beam failure stress.

3.3. Strength measurement results

In the vast majority of the tested specimens we could observe a fracture surface or even the origin of failure (Fig. 3f). Hence, we often know approximately the position along the bent ligament or cantilever beam of the spot where failure initiated. We have therefore evaluated the specimen strength as the value of the first principal stress obtained from FEM simulations at the moment of failure at that location, that is for maximum measured vertical, and lateral force, in C-shaped specimens, or maximum applied force in cantilever beams, at the position of the observed failure. Note that, as the first principal stress distribution along the C-shape specimen bent ligament changes only marginally (Fig. 7d), the error intro-

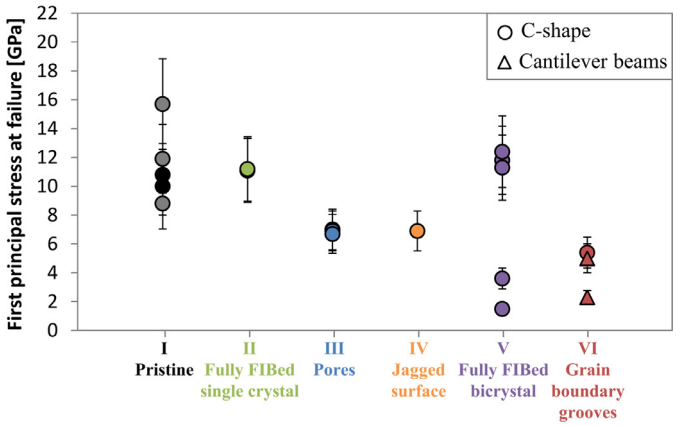

Fig. 9. Summary of results obtained by testing C-shape and micro-cantilever beam specimens of Sumicorundum alumina particles. The vertical axis of the plot represents the first principal stress present in the vicinity of the observed fracture initiation at the moment of failure. Specimens are sorted along the horizontal axis by category. Two fully black circles for Category I represent specimens for which the fracture surface could be observed and for which the stress in the vicinity of the observed failure is reported, while the three gray circles represent specimens for which the fracture surface was likely not apparent; for these three specimens, the reported failure stress value is the peak first principal stress in the ligament at the moment of failure.

duced due to the imprecision in the determination of failure position is smaller than the error due to imprecisions in the measurement of specimen dimensions (less than 10%).

The strength measurement results are presented in Fig. 9. The results are sorted along the horizontal axis of the plot according to the specimen category, while the *y*-axis represents the value of the measured strength for each sample. Based on a sensitivity analysis the reported strength values are precise within 20%, which defines magnitudes of the error bars.

As mentioned previously, in three C-shape specimens of Category I (pristine surface) the site of the failure could not be determined, visibly due to the initiation and propagation of secondary cracks. Hence, for these three specimens, not knowing the exact failure initiation site, we took simply the peak value of the first principal stress within the ligament at the moment of failure as the failure stress. The results from these three specimens are indicated in the plot using the color gray. Measured strength values are also given in Tables S1 and S2 in the Supplementary information.

4. Discussion

4.1. Precision of data

Most of the present specimens were prepared by deep etching a polymer composite containing Sumicorundum alumina particles, using the so-called “piranha solution”. This raises the question of a potential effect on alumina properties of the etching procedure; we investigated the matter by means of nanoindentation. The reduced modulus of polished Sumicorundum alumina particles embedded in a matrix of copper was evaluated before and after exposure of the alumina surface to the etchant for durations similar to those used in sample preparation. No significant difference was found in the nanoindentation behavior between particles with or without exposure. Results are given in Supplementary information, Section S5. Moreover, the alumina particle obtained by cleaving the epoxy matrix gave a similar result as particles that were subjected to etching. A similar comparison of alumina nanoindentation properties before and after exposure to the etchant was additionally performed using samples of dense alumina (to preclude any effect of the matrix); again results showed no influence of the etching procedure on the properties of the alumina phase along its surface.

We do not expect significant plastic deformation to have taken place in our tests, justifying the use of elasticity in mechanical analysis of the samples’ deformation. This is substantiated by (i) the absence of any hysteresis in unload–reload loops that were conducted up to roughly 5 GPa of applied stress in tested C-shape specimens (a representative load–displacement curve is shown in Fig. 3d), (ii) the absence within the fractured ligaments of signs of large scale plasticity such as slip bands (iii) the absence in the literature of hard evidence for room-temperature plasticity in alumina at or below stresses (compressive or tensile) around 10 GPa. In more detail, one study (Montagne et al., 2014) reported plasticity in FIB machined alumina micropillars at room temperature to be initiated only at uniaxial compressive stresses above 11 GPa. In another study (Wang et al., 2013) no significant dislocation activity was observed in nanometric alumina whiskers tested in bending in-situ in the TEM, up to the theoretical strength of sapphire, near 40 GPa.

The sensitivity of the computed stress field on principal test parameters, namely notched specimen geometry, possible misalignments and values of elastic constants used in the model, was analyzed by performing a series of calculations in which each parameter was perturbed by a finite amount, one parameter at a time, starting with the reference configuration of measured dimensions of a typical representative specimen. Details are presented in the Supplementary information; the conclusion is that errors in measurements of dimensions, misalignments and other parameters combined can lead strength

values reported here to be over- or under-estimated by up to 20% of the reported values. Those are therefore magnitudes of the error bars used in Fig. 9.

4.2. Near-theoretical strength in pristine particle regions

Measured strength values for Sumicorundum alumina particles, between 9 and 16 GPa in pristine Category I specimens, are consistent with strength results reported for nearly perfect single crystal α-alumina whiskers. These values exceed what is reported for (flaw-dominated) nanocrystalline high-strength alumina fibers (Wilson, 1997; Žagar et al., 2015) or for a few hundred nanometer thick alumina platelets used in bio-inspired composites (Feilden et al., 2017).

More specifically, reported strengths of high-perfection α-alumina whiskers in air at room temperature, for whiskers of radius ca. 3 μm prepared using different methods (wet hydrogen process or vapor condensation method), typically lie between 7 and 14 GPa (Bayer and Cooper, 1967a; Brenner, 1962; Regester et al., 1967). Similar values, 7–12 GPa, were reported for α-alumina needles of comparable size (Webb and Forgeng, 1958). No prominent dependence of the alumina microcrystal strength on crystal orientation has been reported in the literature, although in one study somewhat higher strength values for A-type ($\langle$hk.0$\rangle$) whiskers were reported compared to C-type ($\langle$0001$\rangle$) whiskers (Regester et al., 1967). Alumina strengths higher than those reported in this study or for microscopic whiskers were achieved only for alumina whiskers a few tens of nanometers in diameter (Wang et al., 2013). The reported strength of these nanoscale whiskers is on the order of 40 GPa and are consistent with the theoretical strength of alumina (Wiederhorn, 1969). The study of Wang et al. (2013) also justifies the use of the purely elastic analysis as these authors did not detect any significant plastic deformation for alumina whiskers approaching theoretical strength in bending.

The measured average local strength of the pristine particle specimens and whiskers of comparable size, on the order of 10 GPa, translate to a critical defect in the shape of a half penny-shape surface crack of radius c = 50–60 nm, if one uses the linear elastic fracture mechanics expression $c = (\frac{K_{IC}}{Y \cdot \sigma_0})^2$ with a fracture toughness, K_{IC}, of single-crystal α-alumina in the range 2.5–3 MPa m$^{1/2}$ (Dörre and Hübner, 1984) and a geometric factor, $Y = 0.66 \cdot \sqrt{\pi}$ for a half-penny shape surface flaw of negligible size with respect to the size of the specimen. Such flaws are at the limit of today's capabilities of SEM imaging, and we were indeed not able to directly identify crack-initiating flaws in Category I particles. Only indirect fracture surface features (river patterns) that pointed to the (featureless) location of failure initiation could be observed. Bayer and Cooper (1967b), based on the observation that whiskers with chemically polished and unpolished surface behave in qualitatively similar manner when their fracture stress exceeds 8–10 GPa, suggested that such strong crystals may fail by crack nucleation induced by dislocation motion (pile-up or dislocation interaction) regardless of the whisker orientation. This may rationalize the fact that no apparent flaws could be observed on the fracture surfaces of Category I specimens in the present work.

Fully FIB-milled specimens with no apparent defects (Category II) exhibited the same fracture stress as (pristine surface) particles of Category I. This observation suggests that either (i) FIB-machining does not alter the nature of the failure initiation of the present particles or alternatively that (ii) FIB-machining introduces such surface defects that the strength of the particles is in the end the same as that of the pristine (FIB unaffected) surface. The FIB affected layer in alumina irradiated by 30 kV Ga^{3+} ions has been studied in HRTEM (Norton et al., 2015), to find that the main FIB artifact is the Ga-implantation of a thin 20 nm layer while the crystalline character of the lattice remains unchanged. The implantation by Ga^{3+} leads to high compressive residual stresses within the implanted layer, estimated to be on the order of 12–15 GPa (Norton et al., 2015). Hence, failure initiation in the fully FIB machined specimens most probably takes place in the underlying material unaffected by the focused ion beam, which in turn may be under considerable tension up to a certain distance from the FIB affected surface in compression. The estimated critical defect size, on the order of 50 nm, is in any event larger than the depth of the implanted layer. Hence, the observation that similar strength values are found in specimens with pristine surfaces or fully FIB-machined specimens, is consistent with a scenario in which fracture nucleates at a flaw or substructure-induced stress concentration site situated at some distance below the original particle surface.

4.3. Strength-limiting defects

One of the observed flaws present in the Sumicorundum alumina particles consisted in microscopic pores, a few tens to a few hundred nanometers in diameter. As seen in Fig. 9, the strength of specimens that contained pores was lower than that of pristine surface specimens by a factor around 2. This is in excellent agreement with the known stress concentration factor of surface or subsurface pores in a fully elastic body (Xu et al., 2012). Here again the fact that similar strengths were observed for two samples with pores present along their FIB-machined ligament back-surface and one specimen with a subsurface pore unaffected by FIB (Fig. S2 in the Supplementary information) suggests that FIB damage did not affect measured strength results in the present material.

Another observed stress concentrator in the present particles is the presence of a jagged surface along some facets, the origin of which is likely a series of parallel twins intersecting the particle free surface. One such tested C-shaped specimen (IV-1) had a strength approximately two times lower than that of Category I specimens. A separate FEM analysis of Specimen IV-1, modeled with a jagged surface and sharp corners of radius 0.2 μm, showed that the local stress concentration at the root of the notch formed by twinned surface, can be up to 2.5 compared to a model with a flat ligament surface with an average specimen width w. Simple stress concentration factors thus again explain the observed failure stress reduction.

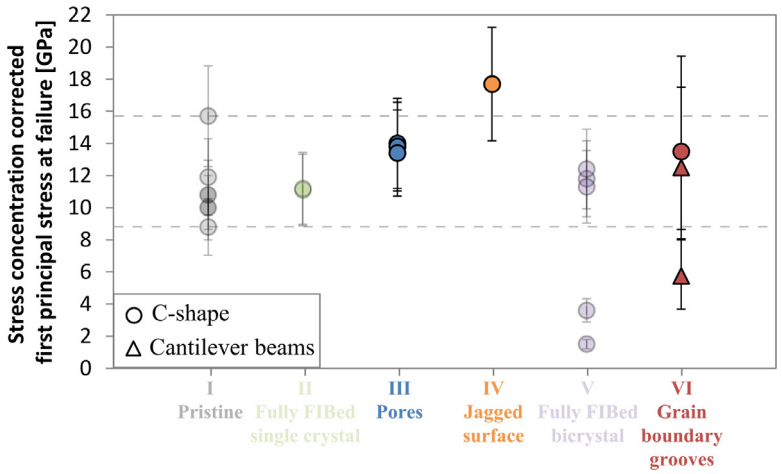

Fig. 10. Strength values for Categories III, IV and VI corrected for the corresponding stress concentration factor, namely $k_t = 2$ for spherical pores, $k_t \approx 2.5$ for a jagged surface calculated from separate FEM simulation and approximately $k_t \approx 2$–3 for realistic geometry of the present grain boundary grooves from (Pilkey and Pilkey, 2008). Measured values for Categories I, II and V with no visible defects are plotted along as partially transparent symbols. Note that the correction for the jagged surface sample is the value of maximum principal stress in the root of the twinned jagged surface notch; however, the exact location of failure (at the scale of the strong stress gradient around the notch root) is unknown, thus the value presented is an upper bound. In the case of grain boundary grooves, symbols represent correction with the average estimated stress concentration of 2.5 and the uncertainty in this factor (which can be between 2 and 3) translates into bigger error bars.

The most deleterious strength-limiting defect in Sumicorundum alumina particles is, by far, the grain boundary. All three tested specimens (one in C-shape configuration and two micro-cantilever beams) from Category VI, which contained a grain boundary groove along a surface unaffected by focused ion beam milling, exhibited strength values well below those reported for Category I particles. The weakest specimen also contained a pore along the revealed grain boundary, and exhibited a local strength value of approximately 2.3 GPa; this is roughly 5 times lower than the strength of Categories I and II specimens. Separate estimations of the stress concentration due to the presence of the grain boundary grooves idealized as notches with a measured values for the root radius and depth indicate that the corresponding stress concentration factor is roughly 2–3 (Pilkey and Pilkey, 2008): hence, the sole presence of grain boundary grooves does not explain the observed drop in strength. To present this quantitatively, Fig. 10 shows the stress-concentration-corrected first principal stress at failure for specimens of Categories III (pores), IV (jagged surface), and VI (grain boundary grooves). As seen, all samples then fall in a band of measured strength values between 8 and 16 GPa, exception made for some of the samples that contained a grain boundary, which fall below that band.

We have therefore performed separate tests on specimens containing individual grain boundaries within the C-shape specimen ligament after machining off the grain boundary groove so as to leave the ligament back-surface flat, thus eliminating the geometrical cause for stress concentration and essentially performing microscopic fracture test of randomly oriented flat alumina bicrystals (sample Category V). The strength results exhibit a high variability, showing that the presence of a grain boundary does not weaken the particle *per se*. Rather, in three out of five specimens, the measured strength was essentially the same as for pristine Category I single crystal specimens; however, in two such specimens the strength fell by a factor of more than five. Fig. 10 thus underlines the deleterious effect of grain boundaries on the intrinsic particle strength. All single-crystalline particles exhibit comparable strengths when corrected for the stress concentrating effect of the observed flaws, whereas for three out of eight particles containing a grain-boundary the stress-concentration-corrected strength is significantly reduced.

This shows first that grain boundaries are the most potent cause for the reduction in strength of Sumicorundum particles, of greater potency than geometrical features that also exist along the surface of those particles. Results also show that the strength of alumina bicrystals is strongly dependent on the crystal orientations; possible underlying reasons for this include effects of (i) elastic anisotropy (Gagorik et al., 1971; Peralta et al., 1993) and/or (ii) residual stresses due to thermal expansion anisotropy (Mar and Scott, 1970).

5. Conclusion

Microscopic C-shaped specimen and cantilever beam tests are developed to measure the local mechanical strength of hard reinforcing particles of low-aspect ratio. The methods provide strength data free of FIB-induced damage, as the particle surface probed in tension may be left pristine. Combining bespoke finite element analysis and fractography, the method yields measurements of the local stress at the place of the fracture initiation with an estimated relative error of 20%, mainly due to uncertainties in specimen dimensions and alignment.

The approach is used to measure the local strength of individual Sumicorundum α-alumina particles that were previously shown to perform well as a reinforcement in metal matrix composites. The results show that alumina particles free of visible defects exhibit very high local strength values, on the order of 10 GPa, similar to values measured on high-perfection alumina whiskers of comparable size.

When such particles contain microstructural flaws, namely micro-pores, surface irregularities, grain boundaries or grain boundary grooves, their strength strongly diminishes. The relative drop in strength caused by pores and surface irregularities is on the order of their associated stress concentration factor, near 2. The most detrimental observed flaws are associated with grain boundaries; these can diminish the local particle strength more than fivefold, down to roughly 2 GPa.

Pooling results, the study shows that the pathway to higher strength α-alumina particles is the elimination of grain boundaries within the particles or alternatively the production of nanocrystalline particles, in which each grain boundary represents but a small flaw. Should one of these be achieved it is possible that remarkably strong and tough metal matrix composites could be produced.

Acknowledgment

This research was funded by the European Research Council under the European Union's Seventh Framework Programme (FP/2007–2013)/ERC Advanced Grant Agreement no. 291085. Scanning electron microscopy and focused ion beam milling was performed at the Interdisciplinary Centre of Electron Microscopy at the École Polytechnique Fédérale de Lausanne (CIME-EPFL).

Appendix. Details of specimen preparation and testing

Carbon coating

The sample of polymer with partially embedded particles was prior to FIB milling coated with thermally evaporated carbon using a Cressington^{TM} Carbon Coater (Watford, England, UK). This produces a relatively weak (owing to low carbon ion energies associated with thermal evaporation (Lifshitz, 1999; Robertson, 1991; Robertson and O'Reilly, 1987)) roughly 40 nm thick carbon layer measured by the high resolution thickness monitor system MTM-10 (Cressington ^{TM}, Watford, England, UK) supplied with the carbon coater. Although the partially embedded particles present a rather complicated topography, their surface is in principle coated uniformly because evaporated carbon films are known to produce highly uniform deposits, even along surfaces that are hidden from lines of sight emanating from the carbon source (Watt, 1985).

C-shaped particle FIB machining

FIB machining of partially-embedded and carbon-coated alumina particles was performed in a Zeiss NVision^{TM} 40 (Oberkochen, Germany) dual beam (SEM/FIB) instrument using a 30 kV Ga^{3+} ion beam. Micromachining was done in such a way that one of the flat facets of the polyhedral particle to be tested was left intact and served as the back surface of the tested C-shape specimen ligament.

The FIB machining process, outlined in Fig. A1, comprised the following steps:

– First, roughly vertical (relative to the polymer matrix free surface to which the particle is embedded) sides of the to-be-formed ligament are machined. This can be done either with the focused ion beam arriving roughly perpendicular to the

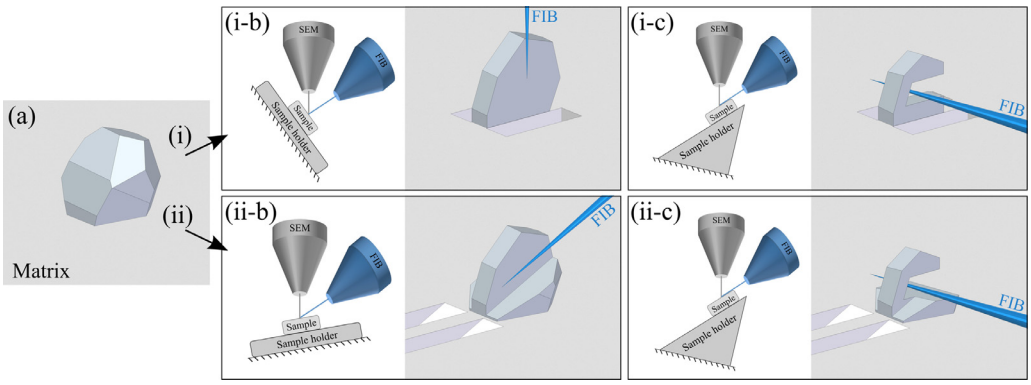

Fig. A1. Two ways to FIB machine a notched specimen from a polyhedral particle (a) partially embedded in a matrix to test in C-shape configuration, by bending a ligament of rectangular cross-section. The particle sides are first machined either (i) with a FIB beam roughly perpendicular to the free surface of the matrix (i-b) or (ii) sideways with the FIB beam at a shallow angle (26°) (ii-b). The last step of a notched specimen preparation involves machining of the wide rectangular notch and single-edge roof, again using the FIB beam, oriented at a very shallow angle (2°–5°) roughly perpendicular to the previously machined sides which is identical for both milling strategies (i-c and ii-c).

polymer matrix free surface (Fig. A1(i-b)) or from an opposite side of the selected particle facet, at an incident angle of roughly 26° with respect to the polymer matrix free surface (this being the minimum incident angle when a standard flat SEM pin stub sample holder is used), Fig. A1(ii-b). The advantage of machining at a shallow angle from the opposite side of the to-be-tested ligament back-surface is that when the particle is FIB imaged (as is necessary to perform the milling procedure) one does not expose the carbon-coated ligament surface to ions, thus eliminating any exposure to ions of the probed surface. On the other hand, a redeposited layer, a few tens of nanometers thick, covering the facet surface is formed in this configuration; protecting the particle, and separating its free surface from such redeposited material, was another purpose of the carbon coating that was deposited prior to FIB machining. The formation of a redeposition layer over the selected facet is avoided when machining with a roughly vertical beam incident angle. In this configuration, a small dose of Ga^{3+} may reach the surface of the selected facet during imaging with the focused ion beam; here again the carbon coating protects the facet surface.

- Secondly, a wide rectangular notch is FIB-machined with the beam oriented perpendicular to the previously machined sides (see Fig. A1(i-c) and A1(ii-c)). To this end, the particle-containing sample is mounted on a 45° pin stub sample holder to allow the incident FIB beam to be almost parallel (typically within $+3°$ to $+4°$) to the polymer matrix free surface.
- Finally, a roof situated at the top of the particle and eccentrically placed with respect to the machined ligament is cut, parallel to the notch. The roofline serves as an unambiguous load-line when testing the machined particles using a flat-end diamond tip in an instrumented nanoindeter. FIB currents used ranged from 6.5 nA in initial rough-milling steps down to 1.5 nA in the last milling steps. Prior to testing, each specimen was examined in the SEM in order to measure its characteristic dimensions.

Mechanical testing of individual FIB machined particles was carried out using a TI 950 TriboIndenter™ (Hysitron Corp., Minneapolis, MN, USA) nanoindentation apparatus equipped with (i) a low-load transducer fitted with a sharp (≈1 µm of tip radius) conospherical diamond probe suitable also for Scanning Probe Microscopy (SPM) and (ii) a 3D OmniProbe™ transducer capable of measuring vertical and lateral force simultaneously with a ≈10 µm tip diameter flat-end diamond probe. Prior to testing, the sample containing FIB machined specimens was mounted on top of a single-axis goniometric tilt stage fixed on the nanoindenter base stage, which was used to align the FIB machined specimen roofline parallel to the 3D OmniProbe flat-end diamond probe. To this end, both the specimen roof and flat-end diamond probe indent left in an aluminum sample were scanned using the SPM function of the low-load transducer. The measured misalignment was then corrected using the single-axis goniometric tilt stage within ±0.5° precision such that the load can be applied evenly along the roofline. Once the specimen was aligned the load was applied via the 3D OmniProbe with a flat-end diamond tip using a displacement feedback control with constant displacement rate of 100 nm/s. A few load–unload cycles of amplitude up to 400 nm are first applied before the displacement is ramped up until fracture; this was done in order to verify the good alignment of the specimen and smoothness of the roof sliding along the diamond probe flat-end, features that are betrayed by a consistent friction coefficient (defined here as the lateral to vertical force ratio). After the test, the sample was removed from the nanoindenter and carefully observed in the SEM (Zeiss Merlin, Oberkochen, Germany), notably in order to conduct fractographic analyses of particle remnants. All C-shape tests were done at room temperature and relative humidity ≈ 50 %.

Micrometric bend beams

Sample preparation was, up to FIB machining, identical to that followed to prepare samples for testing in the C-shape test method: the selected particle's sides were first machined with the FIB incident angle roughly perpendicular to the surface of the particle that will form the beam upper surface. Subsequently, the cantilever bottom surface was formed by FIB milling with the beam at a very shallow angle, parallel to the top surface defined by the two facets meeting at the grain boundary (see Fig. 2a,b). The top surface of the cantilever beam, subject to tension during the test, was left unaffected by FIB milling. The machined cantilever beams are mechanically tested in-situ in a Zeiss Merlin™ (Oberkochen, Germany) scanning electron microscope (SEM) using a FemtoTools FT-NMT03 Nanomechanical Testing System (Buchs-ZH, Switzerland) equipped with a sharp tungsten needle mounted on the 100 mN range load cell. This nanomechanical testing apparatus is equipped with a rotational and tilting stage, which was used to align the cantilever upper surface such that it is oriented perpendicular to the tungsten needle axis. Cantilevers were loaded with the tip of the needle close to the cantilever far end, using a constant displacement rate of 10 nm/s, up to failure of the beam. During the test, a video using the incorporated option of Zeiss SmartSEM operating software, was recorded, showing the deformation and moment of fracture of the beam.

Supplementary materials

Supplementary material associated with this article can be found, in the online version, at doi:10.1016/j.jmps.2017.08.005.

References

Babout, L., Maire, E., Fougères, R., 2004. Damage initiation in model metallic materials: X-ray tomography and modelling. Acta Mater. 52, 2475–2487. doi:10.1016/j.actamat.2004.02.001.

Bayer, P.D., Cooper, R.E., 1967a. Size-strength effects in sapphire and silicon nitride whiskers at 20 °C. J. Mater. Sci. 2, 233–237. doi:10.1007/BF00555379.

Bayer, P.D., Cooper, R.E., 1967b. The effects of chemical polishing on the strength of sapphire whiskers. J. Mater. Sci. 2, 347–353. doi:10.1007/BF00572418.
Beremin, F.M., 1981. Cavity formation from inclusions in ductile fracture of A508 steel. Metall. Trans. A 12, 723–731. doi:10.1007/BF02648336.
Bonderer, L.J., Studart, A.R., Gauckler, L.J., 2008. Bioinspired design and assembly of platelet reinforced polymer films. Science 319, 1069–1073. doi:10.1126/science.1148726.
Bouville, F., Maire, E., Meille, S., Van, D.M., Stevenson, A.J., Deville, S., 2014. Strong, tough and stiff bioinspired ceramics from brittle constituents. Nat. Mater. 13, 508–514. doi:10.1038/nmat3915.
Brechet, Y., Embury, J.D., Tao, S., Luo, L., 1991. Damage initiation in metal matrix composites. Acta Metall. Mater. 39, 1781–1786. doi:10.1016/0956-7151(91)90146-R.
Brenner, S.S., 1962. Mechanical behavior of sapphire whiskers at elevated temperatures. J. Appl. Phys. 33, 33. doi:10.1063/1.1728523.
Brockenbrough, J.R., Zok, F.W., 1995. On the role of particle cracking in flow and fracture of metal matrix composites. Acta Metall. Mater. 43, 11–20. doi:10.1016/0956-7151(95)90256-2.
Caceres, C.H., Griffiths, J.R., 1996. Damage by the cracking of silicon particles in an Al-7Si-0.4Mg casting alloy. Acta Mater. 44, 25–33. doi:10.1016/1359-6454(95)00172-8.
Coade, R.W., Griffiths, J.R., Parker, B.A., Stevens, P.J., 1981. Inclusion stresses in a two-phase alloy deformed to a plastic strain of 1%. Philos. Mag. A 44, 357–372. doi:10.1080/01418618108239538.
Dörre, E., Hübner, H., 1984. Alumina: Processing, Properties, And Applications, Materials Research and Engineering. Springer, Berlin.
Eshelby, J.D., 1957. The determination of the elastic field of an ellipsoidal inclusion, and related problems. Proc. R. Soc. Lond. Math. Phys. Eng. Sci. 241, 376–396. doi:10.1098/rspa.1957.0133.
Feilden, E., Giovannini, T., Ni, N., Ferraro, C., Saiz, E., Vandeperre, L., Giuliani, F., 2017. Micromechanical strength of individual Al_2O_3 platelets. Scr. Mater. 131, 55–58. doi:10.1016/j.scriptamat.2017.01.008.
Finlayson, T.R., Griffiths, J.R., Viano, D.M., Fitzpatrick, M.E., Oliver, E.C., Wang, Q.G., 2007. Stresses in the eutectic silicon particles of strontium-modified A356 castings loaded in tension. In: Proceedings of TMS Annual Meeting, pp. 127–134.
Gagorik, J.E., Queeney, R.A., McKinstry, H.A., 1971. Stress distributions in Al_2O_3 bicrystal tensile specimens. J. Am. Ceram. Soc. 54, 625–627. doi:10.1111/j.1151-2916.1971.tb16018.x.
Ghosh, S., Moorthy, S., 1998. Particle fracture simulation in non-uniform microstructures of metal–matrix composites. Acta Mater. 46, 965–982. doi:10.1016/S1359-6454(97)00289-9.
Gurland, J., 1972. Observations on the fracture of cementite particles in a spheroidized 1.05% c steel deformed at room temperature. Acta Metall. 20, 735–741. doi:10.1016/0001-6160(72)90102-2.
Harris, S.J., O'Neill, A., Boileau, J., Donlon, W., Su, X., Majumdar, B.S., 2007. Application of the Raman technique to measure stress states in individual Si particles in a cast Al–Si alloy. Acta Mater. 55, 1681–1693. doi:10.1016/j.actamat.2006.10.028.
Hauert, A., Rossoll, A., Mortensen, A., 2009a. Particle fracture in high-volume-fraction ceramic-reinforced metals: governing parameters and implications for composite failure. J. Mech. Phys. Solids 57, 1781–1800. doi:10.1016/j.jmps.2009.08.005.
Hauert, A., Rossoll, A., Mortensen, A., 2009b. Ductile-to-brittle transition in tensile failure of particle-reinforced metals. J. Mech. Phys. Solids 57, 473–499. doi:10.1016/j.jmps.2008.11.006.
Joseph, S., Kumar, S., Bhadram, V.S., Narayana, C., 2015. Stress states in individual Si particles of a cast Al–Si alloy: micro-Raman analysis and microstructure based modeling. J. Alloys Compd. 625, 296–308. doi:10.1016/j.jallcom.2014.10.207.
Kiser, M.T., Zok, F.W., Wilkinson, D.S., 1996. Plastic flow and fracture of a particulate metal matrix composite. Acta Mater. 44, 3465–3476. doi:10.1016/1359-6454(96)00028-6.
Kouzeli, M., Weber, L., San Marchi, C., Mortensen, A., 2001. Influence of damage on the tensile behaviour of pure aluminium reinforced with $\geq$40 vol. pct alumina particles. Acta Mater. 49, 3699–3709. doi:10.1016/S1359-6454(01)00279-8.
Krüger, C., Mortensen, A., 2014. Infiltrated Cu_8Al–Ti alumina composites. Compos. Part Appl. Sci. Manuf. 66, 1–15. doi:10.1016/j.compositesa.2014.06.019.
Le Ferrand, H., Bouville, F., Niebel, T.P., Studart, A.R., 2015. Magnetically assisted slip casting of bioinspired heterogeneous composites. Nat. Mater. 14, 1172–1179. doi:10.1038/nmat4419.
Lewandowski, J.J., Liu, C., Hunt Jr., W.H., 1989. Effects of matrix microstructure and particle distribution on fracture of an aluminum metal matrix composite. Mater. Sci. Eng. A, Proceedings of the Symposium on Interfacial Phenomena in Composites: Processing Characterization and Mechanical Properties 107, 241–255. doi:10.1016/0921-5093(89)90392-4.
Lewis, C.A., Withers, P.J., 1995. Weibull modelling of particle cracking in metal matrix composites. Acta Metall. Mater. 43, 3685–3699. doi:10.1016/0956-7151(95)90152-3.
Lifshitz, Y., 1999. Diamond-like carbon — present status. Diam. Relat. Mater. 8, 1659–1676. doi:10.1016/S0925-9635(99)00087-4.
Li, M., Ghosh, S., Richmond, O., 1999. An experimental–computational approach to the investigation of damage evolution in discontinuously reinforced aluminum matrix composite. Acta Mater. 47, 3515–3532. doi:10.1016/S1359-6454(99)00148-2.
Llorca, J., Martin, A., Ruiz, J., Elices, M., 1993. Particulate fracture during deformation of a spray formed metal-matrix composite. Metall. Trans. A 24, 1575–1588. doi:10.1007/BF02646597.
Majumdar, B.S., Pandey, A.B., 2000. Deformation and fracture of a particle-reinforced aluminum alloy composite: part II. Modeling. Metall. Mater. Trans. A 31, 937–950. doi:10.1007/s11661-000-0036-z.
Mar, H.Y.B., Scott, W.D., 1970. Fracture induced in Al_2O_3 bicrystals by anisotropic thermal expansion. J. Am. Ceram. Soc. 53, 555–558. doi:10.1111/j.1151-2916.1970.tb15965.x.
Miserez, A., Mortensen, A., 2004. Fracture of aluminium reinforced with densely packed ceramic particles: influence of matrix hardening. Acta Mater. 52, 5331–5345. doi:10.1016/j.actamat.2004.07.038.
Miserez, A., Müller, R., Mortensen, A., 2006. Increasing the strength/toughness combination of high volume fraction particulate metal matrix composites using an Al–Ag matrix alloy. Adv. Eng. Mater. 8, 56–62. doi:10.1002/adem.200500185.
Miserez, A., Müller, R., Rossoll, A., Weber, L., Mortensen, A., 2004a. Particle reinforced metals of high ceramic content. Mater. Sci. Eng. A, 13th International Conference on the Strength of Materials 387–389, 822–831. doi:10.1016/j.msea.2004.05.054.
Miserez, A., Rossoll, A., Mortensen, A., 2004b. Fracture of aluminium reinforced with densely packed ceramic particles: link between the local and the total work of fracture. Acta Mater. 52, 1337–1351. doi:10.1016/j.actamat.2003.11.019.
Mochida, T., Taya, M., Lloyd, D.J., 1991. Fracture of particles in a particle/metal matrix composite under plastic straining and its effect on the Young's modulus of the composite. Mater. Trans. JIM 32, 931–942. doi:10.2320/matertrans1989.32.931.
Montagne, A., Pathak, S., Maeder, X., Michler, J., 2014. Plasticity and fracture of sapphire at room temperature: load-controlled microcompression of four different orientations. Ceram. Int. 40, 2083–2090. doi:10.1016/j.ceramint.2013.07.121.
Mueller, M.G., Fornabaio, M., Žagar, G., Mortensen, A., 2016. Microscopic strength of silicon particles in an aluminium–silicon alloy. Acta Mater. 105, 165–175. doi:10.1016/j.actamat.2015.12.006.
Mueller, M.G., Žagar, G., Mortensen, A., 2017. In-situ strength of individual silicon particles within an aluminium casting alloy. Acta Mater. (Submitted for publication).
Mueller, R., Rossoll, A., Weber, L., Bourke, M.A.M., Dunand, D.C., Mortensen, A., 2008. Tensile flow stress of ceramic particle-reinforced metal in the presence of particle cracking. Acta Mater. 56, 4402–4416. doi:10.1016/j.actamat.2008.05.004.
Mummery, P.M., Derby, B., 1994. In situ scanning electron microscope studies of fracture in particulate-reinforced metal-matrix composites. J. Mater. Sci. 29, 5615–5624. doi:10.1007/BF00349956.
Mummery, P.M., Derby, B., Scruby, C.B., 1993. Acoustic emission from particulate-reinforced metal matrix composites. Acta Metall. Mater. 41, 1431–1445. doi:10.1016/0956-7151(93)90252-N.

Munch, E., Launey, M.E., Alsem, D.H., Saiz, E., Tomsia, A.P., Ritchie, R.O., 2008. Tough, bio-inspired hybrid materials. Science 322, 1516–1520. doi:10.1126/science.1164865.
Norton, A.D., Falco, S., Young, N., Severs, J., Todd, R.I., 2015. Microcantilever investigation of fracture toughness and subcritical crack growth on the scale of the microstructure in Al_2O_3. J. Eur. Ceram. Soc. 35, 4521–4533. doi:10.1016/j.jeurceramsoc.2015.08.023.
Ogiso, H., Yoshida, M., Nakano, S., Akedo, J., 2007. Effects of Al ion implantation on the strength of Al_2O_3 particles. Surf. Coat. Technol., SMMIB 2005 14th International Conference on Surface Modification of Materials by Ion Beams 201, 8180–8184. doi:10.1016/j.surfcoat.2006.01.093.
Pandey, A.B., Majumdar, B.S., Miracle, D.B., 2000. Deformation and fracture of a particle-reinforced aluminum alloy composite: part I. Experiments. Metall. Mater. Trans. A 31, 921–936.
Peralta, P., Schober, A., Laird, C., 1993. Elastic stresses in anisotropic bicrystals. Mater. Sci. Eng. A 169, 43–51. doi:10.1016/0921-5093(93)90597-8.
Pilkey, W.D., Pilkey, D.F., 2008. Peterson's Stress Concentration Factors, 3rd ed. John Wiley & Sons.
Regester, R.F., Gorsuch, P.D., Girifalco, L., 1967. Structure and properties of aluminum oxide whiskers. Nav. Eng. J. 79, 957–960. doi:10.1111/j.1559-3584.1967.tb05383.x.
Robertson, J., 1991. Hard amorphous (diamond-like) carbons. Prog. Solid State Chem. 21, 199–333. doi:10.1016/0079-6786(91)90002-H.
Robertson, J., O'Reilly, E.P., 1987. Electronic and atomic structure of amorphous carbon. Phys. Rev. B 35, 2946–2957. doi:10.1103/PhysRevB.35.2946.
Scarber, P., Janowski, G.M., 2001. Finite element analysis of reinforcement particle cracking in Al/SiCp composites. Mater. Sci. Technol. 17, 1339.
Sedmák, P., Pilch, J., Heller, L., Kopeček, J., Wright, J., Sedlák, P., Frost, M., Šittner, P., 2016. Grain-resolved analysis of localized deformation in nickel–titanium wire under tensile load. Science 353, 559–562. doi:10.1126/science.aad6700.
Strobl, S., Supancic, P., Schöppl, O., Danzer, R., 2014. A new strength test for ceramic cylinders—the notched roller test. J. Eur. Ceram. Soc. 34, 2575–2584. doi:10.1016/j.jeurceramsoc.2014.02.009.
Supancic, P., Danzer, R., Witschnig, S., Polaczek, E., Morrell, R., 2009. A new test to determine the tensile strength of brittle balls—the notched ball test. J. Eur. Ceram. Soc. 29, 2447–2459. doi:10.1016/j.jeurceramsoc.2009.02.018.
Tekoglu, C., Pardoen, T., 2010. A micromechanics based damage model for composite materials. Int. J. Plast. 26, 549–569. doi:10.1016/j.ijplas.2009.09.002.
Uchida, Y., Sawabe, Y., Mohri, M., 1995. Nearly monodispersed single crystal particles of alpha-alumina. In: Science, Technology, and Applications of Colloidal Suspensions. Presented at the 96th Annual Meeting of the American Ceramic Society. The American Ceramic Society, Indianapolis, IN, United States, pp. 159–165.
Wachtman, J.B., Tefft, W.E., Lam, D.G., Stinchfield, R.P., 1960. Elastic constants of synthetic single-crystal corundum at room temperature. J. Am. Ceram. Soc. 64A, 213–228.
Wallin, K., Saario, T., Törrönen, K., 1986. Fracture of brittle particles in a ductile matrix. Int. J. Fract. 32, 201–209. doi:10.1007/BF00018353.
Wang, Q.G., 2004. Plastic deformation behavior of aluminum casting alloys A356/357. Metall. Mater. Trans. A 35, 2707–2718. doi:10.1007/s11661-004-0216-3.
Wang, Q.G., Caceres, C.H., Griffiths, J.R., 2003. Damage by eutectic particle cracking in aluminum casting alloys A356/357. Metall. Mater. Trans. A 34, 2901–2912. doi:10.1007/s11661-003-0190-1.
Wang, S., He, Y., Huang, H., Zou, J., Auchterlonie, G.J., Hou, L., Huang, B., 2013. An improved loop test for experimentally approaching the intrinsic strength of alumina nanoscale whiskers. Nanotechnology 24, 285703. doi:10.1088/0957-4484/24/28/285703.
Watt, I.M., 1985. The Principles and Practice of Electron Microscopy. Cambridge University Press, Cambridge [Cambridgeshire], New York.
Webb, W.W., Forgeng, W.D., 1958. Mechanical behavior of microcrystals. Acta Metall. 6, 462–469. doi:10.1016/0001-6160(58)90109-3.
Wereszczak, A.A., Jadaan, O.M., Lin, H.-T., Champoux, G.J., Ryan, D.P., 2007a. Hoop tensile strength testing of small diameter ceramic particles. J. Nucl. Mater. 361, 121–125. doi:10.1016/j.jnucmat.2006.11.013.
Wereszczak, A.A., Kirkland, T.P., Jadaan, O.M., 2007b. Strength measurement of ceramic spheres using a diametrally compressed "C-Sphere" specimen. J. Am. Ceram. Soc. 90, 1843–1849. doi:10.1111/j.1551-2916.2007.01639.x.
Wiederhorn, S.M., 1969. Fracture of sapphire. J. Am. Ceram. Soc. 52, 485–491.
Wilson, D.M., 1997. Statistical tensile strength of NextelTM 610 and NextelTM 720 fibres. J. Mater. Sci. 32, 2535–2542. doi:10.1023/A:1018538030985.
Xu, Z., Wen, W., Zhai, T., 2012. Effects of pore position in depth on stress/strain concentration and fatigue crack initiation. Metall. Mater. Trans. A 43, 2763–2770. doi:10.1007/s11661-011-0947-x.
Yoshida, M., Ogiso, H., Nakano, S., Akedo, J., 2005. Compression test system for a single submicrometer particle. Rev. Sci. Instrum. 76, 093905. doi:10.1063/1.2038187.
Žagar, G., Pejchal, V., Mueller, M.G., Rossoll, A., Cantoni, M., Mortensen, A., 2015. The local strength of microscopic alumina reinforcements. Acta Mater. 100, 215–223. doi:10.1016/j.actamat.2015.08.026.